

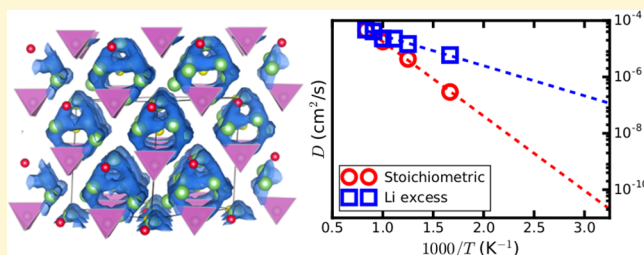
Data-Driven First-Principles Methods for the Study and Design of Alkali Superionic Conductors

Zhi Deng, Zhuoying Zhu, Iek-Heng Chu, and Shyue Ping Ong*

Department of NanoEngineering, University of California San Diego, 9500 Gilman Drive, Mail Code 0448, La Jolla, California 92093-0448, United States

S Supporting Information

ABSTRACT: We present a detailed exposition of how first-principles methods can be used to guide alkali superionic conductor (ASIC) study and design. Using the argyrodite $\text{Li}_6\text{PS}_5\text{Cl}$ as a case study, we demonstrate how modern information technology (IT) infrastructure and software tools can facilitate the assessment of alkali superionic conductors in terms of various critical properties of interest such as phase and electrochemical stability and ionic conductivity. The emphasis is on well-documented, reproducible analysis code that can be readily generalized to other material systems and design problems. For our chosen $\text{Li}_6\text{PS}_5\text{Cl}$ case study material, we show that Li excess is crucial to enhancing its conductivity by increasing the occupancy of interstitial sites that promote long-range Li^+ diffusion between cage-like frameworks. The predicted room-temperature conductivities and activation barriers are in reasonably good agreement with experimental values.



INTRODUCTION

All-solid-state rechargeable alkali-ion batteries utilizing an alkali superionic conductor (ASIC) electrolyte are a highly promising energy storage architecture that is both safer and potentially more energy dense than traditional organic liquid electrolyte-based architecture. A ceramic ASIC is nonflammable and can be stacked with the electrodes to achieve higher system-level energy densities.^{1–3}

Significant progress has been made in the development of ASICs with excellent room-temperature ionic conductivities. For example, the $\text{Li}_{10}\text{GeP}_2\text{S}_{12}$ family of superionic conductors have room-temperature ionic conductivities in the range of 4–25 mS/cm,^{4–7} rivaling that of traditional liquid electrolytes. Similar conductivities have been achieved in the Na_3PS_4 superionic conductor and its derivatives.^{8–11} Oxide alkali superionic conductors such as the garnet LLZO ($\text{Li}_7\text{La}_3\text{Zr}_2\text{O}_{12}$),¹² perovskite LLTO (lithium lanthanum titanium oxide),¹³ and NASICONs (NAtrium SuperIonic CONductors)¹⁴ typically have conductivities about an order of magnitude lower than the sulfides.

First-principles methods based on density functional theory (DFT) are an invaluable complementary toolkit to experiments in the understanding and design of battery materials, including ASICs.^{15–17} For instance, DFT studies first clarified the 3D diffusion topology in $\text{Li}_{10}\text{GeP}_2\text{S}_{12}$ and suggested the Si and Sn analogues that are significantly cheaper and have similar conductivities.^{18,19} DFT methods can also be used to provide insights into the performance limits and potential doping strategies to tune carrier concentration and diffusion barriers.^{9,20,21}

In this work, we provide a detailed exposition of how DFT methods can be used to guide ASIC study and design.^{22–26} We will use the argyrodite $\text{Li}_6\text{PS}_5\text{Cl}$ superionic conductor^{22–26} as a case study, though the methods discussed are broadly applicable. We will present a holistic approach to ASIC study and design, which focuses not only on the ionic conductivity as a design parameter but also on other technologically relevant properties such as phase and electrochemical stability. The emphasis is on the use of modern information technology (IT) and database infrastructure coupled with robust software packages to efficiently conduct and analyze DFT calculations. It should be noted that, while ASICs are the chosen application of focus, similar considerations and approaches apply to many materials design problems, e.g., fast oxygen ionic conductors for solid oxide fuel cells,²⁷ battery cathodes, etc.

SOFTWARE CODES USED

All DFT calculations in this work were performed using the Vienna *Ab initio* Simulation Package (VASP)²⁸ within the projected augmented wave approach.²⁹ However, the types of calculations performed are available in most mature electronic structure calculation packages, and the same analysis can be applied with minor modifications. The Perdew–Burke–Ernzerhof (PBE) generalized gradient approximation (GGA)³⁰ was adopted for the exchange–correlation functional. Due to vastly different convergence and computational cost

Special Issue: Methods and Protocols in Materials Chemistry

Received: June 30, 2016

Revised: August 3, 2016

requirements, other parameter choices will be discussed in the context of the various types of analysis in subsequent sections.

The primary analysis software used is the Python Materials Genomics (pymatgen) library,³¹ an open source materials analysis library that facilitates many of the structure manipulations, input file generations, and analyses performed. Detailed installation instructions are available on the official pymatgen website (<http://pymatgen.org/>). Some of the analyses (e.g., van Hove function, probability density function) have been implemented in an open-source add-on package, pymatgen-diffusion.³² All analysis examples are written in the Python programming language and presented in Jupyter notebooks³³ available in the [Supporting Information](#).

■ STRUCTURE GENERATION AND RELAXATION

In most studies, the initial crystal structure is typically obtained from experimental sources, such as the Inorganic Crystal Structure Database (ICSD).³⁴ However, many ASIC crystal structures (e.g., $\text{Li}_{10}\text{GeP}_2\text{S}_{12}$, cubic Na_3PS_4) exhibit disorder. Therefore, an enumeration of all symmetrically distinct atomic configurations must first be carried out and their energies calculated to identify the lowest energy ordering (or at the least, a reasonably low energy ordering).

Practical Considerations. Enumeration of disordered structures is fundamentally a trade-off between computational cost and completeness. The larger the supercell size used for enumeration, the higher is the likelihood that the ground state ordering will be found. However, due to combinatorial explosion, complete enumeration of all symmetrically distinct orderings is performed only using relatively small cell sizes, typically the primitive cell if possible. If complete enumeration is not computationally tractable, some random sampling approach may be used. For *ab initio* molecular dynamics simulations (see later section), only a reasonably low energy ordering is needed as an input structure, and it is not critical that the exact ground state ordering is found.

Example. [Notebook 1](#) shows the enumeration procedure for $\text{Li}_6\text{PS}_5\text{Cl}$. The initial structure obtained from the ICSD (collection code 418490) is a conventional cubic $F43m$ cell with formula $\text{Li}_{6.72}\text{PS}_5\text{Cl}$, i.e., excess of lithium. To obtain stoichiometric charge-balanced $\text{Li}_6\text{PS}_5\text{Cl}$, we adjusted the occupancy of Li 48h sites to 0.5 and enumerated all symmetrically distinct orderings of the *primitive* cell using pymatgen's wrapper to Hart and Forcade's enumlib,³⁵ an efficient Fortran code for enumeration of structure derivatives. A total of 48 unique structures were obtained and fully relaxed using DFT calculations. Although it has been shown both experimentally and theoretically that $\text{Li}_6\text{PS}_5\text{Cl}$ may exhibit antisite S/Cl disorder,²⁶ no attempt was made to model such disorder to keep the computational costs reasonable. The lowest energy structure is shown in [Figure 1](#) and was used as the input to subsequent calculations and analyses. The relaxed lattice parameter a is 10.1 Å, 2.5% larger than the experimental value.²² This slight overestimation is due to the well-known tendency for the GGA functional to underbind.

■ PHASE AND ELECTROCHEMICAL STABILITY

The necessity for phase stability is a common consideration in almost all materials design problems. The phase stability of a material can be estimated by constructing the relevant multicomponent 0 K phase diagram. For the case of $\text{Li}_6\text{PS}_5\text{Cl}$, one would need to calculate the energies of all known phases in

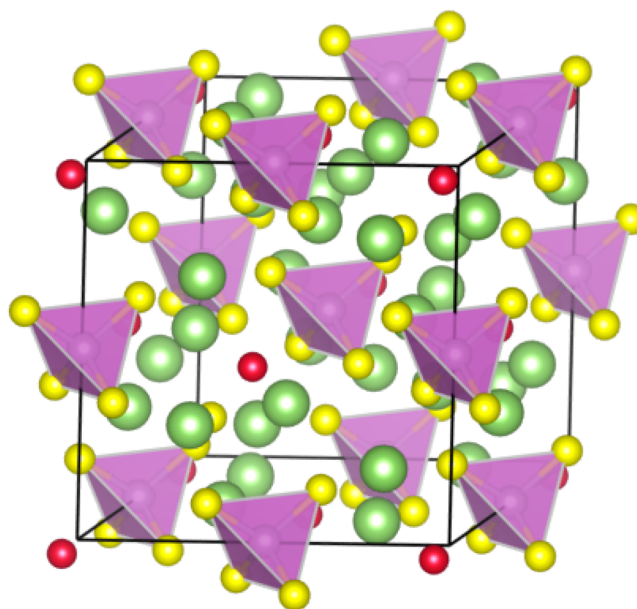


Figure 1. Lowest energy $\text{Li}_6\text{PS}_5\text{Cl}$ structure determined from DFT calculations on all 48 symmetrically distinct orderings of the primitive experimental structure. Li^+ in green, Cl^- in red, S^{2-} in yellow, and PS_4^{3-} polyhedra in purple.

the Li–P–S–Cl chemical space, i.e., all Li, P, S, Cl, Li_xS_y , Li_xP_y , P_xS_y , P_xCl_y , Li_xCl_y , S_xCl_y , $\text{Li}_x\text{P}_y\text{S}_z$, $\text{P}_x\text{S}_y\text{Cl}_z$, $\text{Li}_x\text{S}_y\text{Cl}_z$, $\text{Li}_x\text{P}_y\text{Cl}_z$, and $\text{Li}_x\text{P}_y\text{S}_z\text{Cl}_w$ phases. The phase diagram can then be obtained via constructing the convex hull of the five-dimension (\bar{E} , x_{Li} , x_{P} , x_{S} , x_{Cl}) space, where \bar{E} is the normalized energy per atom, and x_X is the atomic fraction of element X. Finally, the vertices lying on the convex hull³⁶ are projected into the Li–P–S–Cl compositional coordinate space to yield the phase diagram.³⁷ It should be noted that, while finite temperature stability can be estimated by considering various (e.g., vibrational, configurational) contributions to the entropy for all relevant, such a computational and human resource-intensive effort is seldom carried out as the DFT 0K phase diagram typically yields a reasonable initial estimate of the relative stability of crystalline phases.

Another crucial property of an ASIC is its electrochemical stability against the electrodes. This stability can be achieved either intrinsically, i.e., the ASIC being completely inert against both the anode and cathode, or more realistically, via the formation of passivating layers. The phase equilibria at the ASIC/electrode interface may be estimated using a grand potential phase diagram construction.^{4,19} The ASIC is subjected to a maximum range of electrochemical potential when the battery is in a fully charged state (see [Figure 2](#)). Under such conditions, the alkali-depleted cathode is effectively an alkali sink at low alkali chemical potential, while the anode is effectively an alkali source with high alkali chemical potential typically close to that of the bulk alkali metal. Assuming that the alkali ion is the main mobile specie, the ASIC/anode and ASIC/cathode interfaces can be approximated as open systems at $\mu_{\text{A}} = \mu_{\text{A}}^0$ and $\mu_{\text{A}} = \mu_{\text{A}}^0 - e\Delta V$, respectively. Here, μ_{A}^0 is the chemical potential of the bulk alkali metal, e is the elementary charge, and ΔV refers to the voltage of the charged cathode versus A/A^+ .³⁸ The relevant thermodynamic potential at 0 K is therefore the alkali grand potential, given by the following expression:

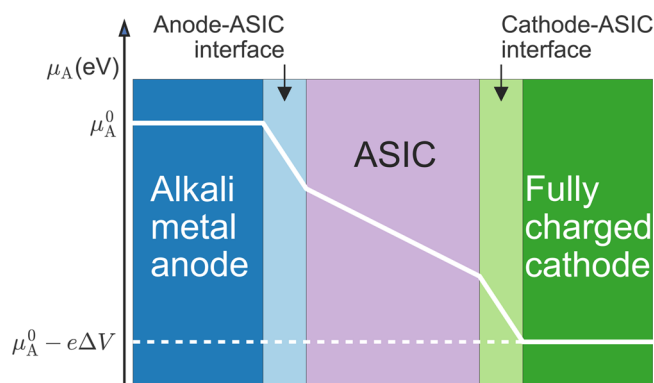


Figure 2. Schematic showing the range of alkali chemical potential (μ_A , indicated by the white lines) in a fully charged all-solid-state alkali-ion battery with an alkali metal anode.

$$\phi = E - \mu_A N_A \quad (1)$$

where E is approximated as the computed DFT energy, N_A is the number of alkali atoms for a particular phase, and the PV term for solids is ignored. Using a similar phase diagram construction with ϕ instead of E , one can examine how the predicted phase equilibria at the ASIC composition changes with alkali chemical potential.

Practical Considerations. Even for a relatively “simple” quaternary compound such as $\text{Li}_6\text{PS}_5\text{Cl}$, a direct phase or electrochemical stability assessment is a significant computational undertaking due to the requirement to compute all phases in the Li-P-S-Cl system. Fortunately, one can leverage on existing large open databases such as the Materials Project (MP),³⁹ which contains the computed energies of all known ordered inorganic materials. Using pymatgen’s high-level interface to the Materials Application Programming Interface,⁴⁰ one can query for the computed energies of all known ordered phases in the Li-P-S-Cl chemical space (see Notebook 2). To enhance the coverage of the phase space, we have also included derived phases obtained via O/S substitution from ordered Li-P-O ternary compounds. The phase diagram can then be constructed using the *phasediagram* package in pymatgen using all available entries (MP + derived + calculated entry for $\text{Li}_6\text{PS}_5\text{Cl}$). Care must be taken to ensure that the calculation parameters, e.g., choice of functional and pseudopotentials, are similar to those used in the MP to ensure compatibility. Pymatgen may be used to generate compatible VASP input files. The key parameters used are spin-polarized calculations with a kinetic energy cutoff of 520 eV, a k -point density of at least 1000/atom, and a carefully calibrated series of Hubbard U values with corresponding correction values for elements with localized d electrons.⁴¹

Example. The phase stability and electrochemical stability analysis for $\text{Li}_6\text{PS}_5\text{Cl}$ is given in Notebook 2.

Figure 3 shows the calculated pseudoternary $\text{Li}_2\text{S-P}_2\text{S}_5\text{-LiCl}$ phase diagram. From the phase diagram, one may compute the energy above hull (E_{hull}) of $\text{Li}_6\text{PS}_5\text{Cl}$. The E_{hull} of a phase is defined as the normalized energy per atom for that phase above the linear combination of stable equilibrium phases at that composition in the phase diagram. A stable compound has an E_{hull} of 0, and the higher the E_{hull} , the more unstable the compound is likely to be. The calculated E_{hull} of $\text{Li}_6\text{PS}_5\text{Cl}$ is 21 meV/atom, indicating that it is metastable with respect to a linear combination of Li_3PS_4 , Li_2S , and LiCl at 0 K.

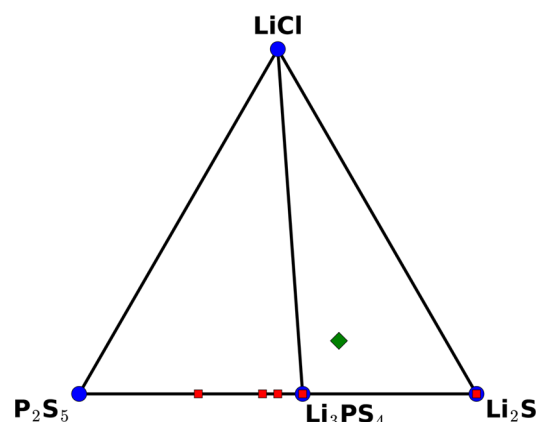


Figure 3. Pseudoternary $\text{Li}_2\text{S-P}_2\text{S}_5\text{-LiCl}$ phase diagram. Blue circles with labeled compositions indicate stable phases. $\text{Li}_6\text{PS}_5\text{Cl}$ is metastable (green diamond). Other unstable/metastable phases (including derived ones from O substitution by S in Li-P-O ternary compounds) are shown as red squares. The compositions of unstable/metastable phases along $\text{P}_2\text{S}_5\text{-Li}_2\text{S}$ are LiPS_3 , $\text{Li}_4\text{P}_2\text{S}_7$, $\text{Li}_7\text{P}_3\text{S}_{11}$, Li_3PS_4 , and Li_2S .

Figure 4 shows the plot of the Li uptake per formula unit (f.u.) of $\text{Li}_6\text{PS}_5\text{Cl}$ against voltage vs Li/Li^+ . At low voltage (high

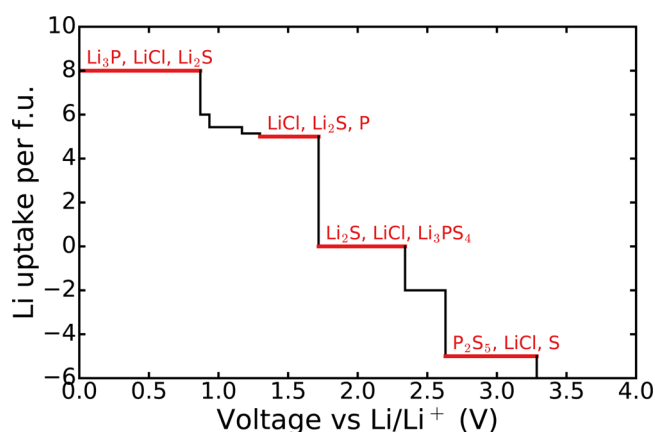


Figure 4. Plot of Li uptake per formula unit (f.u.) of $\text{Li}_6\text{PS}_5\text{Cl}$ solid electrolyte (black solid) against voltage vs Li/Li^+ . At low voltage (high Li chemical potential), $\text{Li}_6\text{PS}_5\text{Cl}$ undergoes reduction and uptakes Li, whereas at high voltage (low Li chemical potential), $\text{Li}_6\text{PS}_5\text{Cl}$ is oxidized and loses Li. Text indicates the predicted phase equilibria at corresponding regions of the profile. Only selected regions are annotated for brevity.

Li chemical potential), the $\text{Li}_6\text{PS}_5\text{Cl}$ solid electrolyte undergoes reduction and uptakes Li, while at high voltage (low Li chemical potential), electrolyte is oxidized and loses Li. The plot clearly illustrates one of the major issues with sulfide-based ASICs, the narrow range of intrinsic electrochemical stability. The $\text{Li}_6\text{PS}_5\text{Cl}$ composition is stable against Li uptake and loss only within a narrow range of voltage (1.7–2.3 V). Nevertheless, we find that electronically insulating, ionically conducting phases (e.g., Li_2S , LiCl) are formed at both higher and lower voltages, which may potentially serve as good passivating interfacial phases that act as a barrier against further ASIC decomposition.

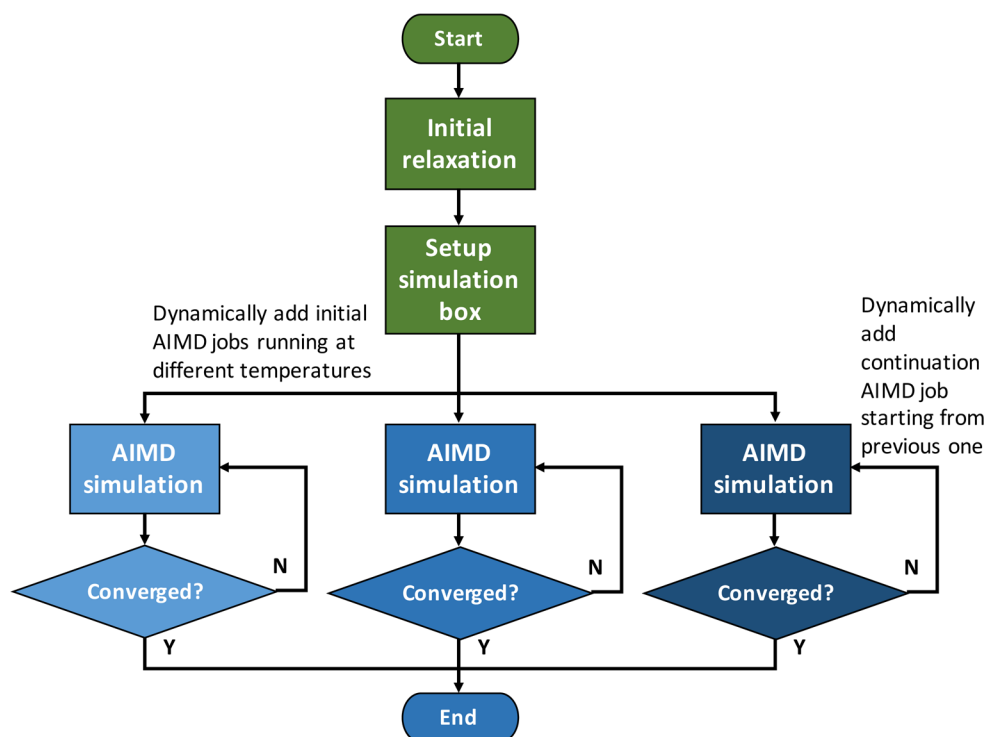


Figure 5. Schematic of the automated AIMD workflow implemented using the FireWorks⁴⁹ workflow software. Processes in the green belong to initial relaxation job. Processes in blue belong to AIMD jobs running in parallel at different temperatures.

■ DIFFUSIVITY AND IONIC CONDUCTIVITY

An ASIC, as its name implies, must have a high alkali ionic conductivity. There are several first-principles approaches to the study of diffusivity and conductivity in materials.¹⁷ The most commonly used approaches are based on transition state methods such as nudged elastic band (NEB) calculations.^{42,43} Though NEB calculations are a powerful tool to extract alkali migration barriers,⁴⁴ such calculations require prior knowledge of the diffusion pathway and are typically performed only at the dilute limits for single vacancy or alkali hops. Modeling ASICs, which have nondilute alkali concentration, with single hops at the dilute limits is usually a poor approximation.¹⁷

A more realistic approach to studying alkali conductivity in ASICs is *ab initio* molecular dynamics (AIMD) simulations. Though highly computationally expensive, recent computing and methodological advances⁴⁵ have rendered AIMD simulations within the reach of modest supercomputing clusters. Furthermore, the expected fast alkali diffusion in ASICs make it more likely that converged diffusion statistics can be obtained with relatively short simulation timeframes compared to slow diffusers.

From an AIMD simulation, the diffusivity can be extracted via the following relation:

$$D = \frac{1}{2dt} \langle [\Delta \mathbf{r}(t)]^2 \rangle \quad (2)$$

where d is the dimensionality factor, which equals 3 for 3-D crystal structure. $\langle [\Delta \mathbf{r}(t)]^2 \rangle$ is the average mean square displacement (MSD) over a time duration t . The diffusivity is usually obtained by performing a linear fitting of the MSD versus $2dt$.

Under the assumption of no phase transitions and an abundance of mobile defect carriers, the diffusivity in a solid generally follows an Arrhenius relationship:

$$D = D_0 \exp\left(-\frac{E_a}{kT}\right) \quad (3)$$

where D_0 is the maximum diffusivity at infinite temperature, E_a is the activation energy, k is the Boltzmann constant, and T is the temperature. To obtain room temperature diffusivity and activation energy, AIMD simulations are performed at multiple temperatures, and an Arrhenius plot of the log of the diffusivity versus $1/T$ is constructed. The alkali ionic conductivity at room temperature $\sigma_{300\text{ K}}$ can then be derived from the Nernst–Einstein equation as follows:

$$\sigma_{300\text{ K}} = \frac{\rho z^2 F^2}{RT} D_{300\text{ K}} \quad (4)$$

where ρ is the molar density of diffusing alkali ions in the unit cell, z is the charge of alkali ions (+1), and F and R are the Faraday's constant and the gas constant, respectively. $T = 300\text{ K}$ was used in the above equation.

Additional insights may be obtained by analyzing the trajectories from the AIMD simulations. A plot of the probability density function $P(\mathbf{r})$ can provide useful information on the low energy (high probability) sites in an ASIC, as well as the migration pathways between them.⁴⁶ P is often defined in a spatial 3D uniform grid and can be computed by averaging the number of the alkali ions at each grid point within a given time scale. P is normalized such that $\int_{\Omega} P d\mathbf{r} = 1$ with Ω being the volume of the unit cell.

Many ASICs also exhibit correlated or cooperative alkali motion, which can be analyzed by computing the van Hove correlation function. The van Hove correlation function can be split into the self-part G_s and the distinct-part G_d as follows:

$$G_s(r, t) = \frac{1}{4\pi r^2 N_d} \left\langle \sum_{i=1}^{N_d} \delta(r - |\mathbf{r}_i(t_0) - \mathbf{r}_i(t + t_0)|) \right\rangle_{t_0} \quad (5)$$

$$G_d(r, t) = \frac{1}{4\pi r^2 \rho N_d} \left\langle \sum_{i \neq j}^{N_d} \delta(r - |\mathbf{r}_i(t_0) - \mathbf{r}_j(t + t_0)|) \right\rangle_{t_0} \quad (6)$$

Here, $\delta(\cdot)$ is the one-dimensional Dirac delta function. The angular bracket stands for the ensemble average over the initial time t_0 . $\mathbf{r}_i(t)$ denotes the position of the i^{th} particle at time t . N_d and r are the number of diffusing alkali ions in the unit cell and radial distance, respectively. The presence of the average number density ρ serves as the “normalization factor” in G_d such that $G_d \rightarrow 1$ when $r \gg 1$. For a given r and t , $G_s(r, t)$ describes how probable a particle diffuses away from its initial position by a distance of r after time t , whereas $G_d(r, t)$ describes the radial distribution of $N - 1$ particles after time t with respect to the initial reference particle. In particular, $G_d(r, t)$ is reduced to the static pair distribution function when $t = 0$, which is often used to investigate the dynamics of structural changes. Both the probability density and van Hove function analyses are already implemented in the open-source `pymatgen-diffusion`³² add-on package.

Practical Considerations. Most AIMD simulations of ASICs are often performed in NVT ensemble with a Nosé-Hoover thermostat.^{47,48} The cell parameters are typically fixed at the 0 K values obtained from DFT structural optimization or at the experimentally reported values. Though this is certainly an approximation in the model, previous studies have found that the resulting diffusivities and conductivities obtained are usually in reasonable agreement with experimental values.^{9,18,19} The choice of the NVT over the NpT ensemble is motivated by the lower computation cost (lower energy cutoff), as well as the fact that simulations can be performed at elevated temperatures to obtain diffusion statistics without melting. Further computational cost savings can be achieved by performing nonspin-polarized calculations with a lower plane-wave energy cutoff and a small k -point mesh. A time step of 2 fs is typically sufficient for simulations of ASIC materials. It should be noted that MD simulations should ideally be performed on large supercells to avoid introducing artificial correlated diffusivity due to periodic boundary conditions. Due to the high cost of AIMD methods, only moderate cell sizes of at least 10 Å in each lattice direction are typically used. Nevertheless, useful statistics and data can usually be obtained even within these limitations.

There are two practical challenges in AIMD simulations. First, most AIMD simulations require multiweek calculations well beyond the wall times of typical supercomputing clusters, and runs have to be performed at multiple temperatures. The traditional approach of performing AIMD simulations therefore requires significant human intervention, with a high likelihood of errors. To address this challenge, we have developed an automated AIMD workflow using FireWorks,⁴⁹ a workflow management software. Figure 5 shows the schematic of a typical AIMD workflow. The crystal structure is first relaxed to an optimized geometry, from which a sufficiently large simulation supercell box is created. Then, AIMD jobs with different targeting temperatures are dynamically added to the workflow. Each AIMD job is running with a `WallTimeHandler` implemented in Custodian library,⁵⁰ which terminates the job gracefully just prior to the wall time limit. A continuation job is then resubmitted until a predefined set of convergence criteria (e.g., a maximum number of time steps, a required MSD, a required R-squared for the MSD vs $2dt$ linear fitting, etc.) is reached. Using this workflow, AIMD simulations can be

performed with minimal human intervention except for an initial workflow and structure setup.

Second, compared to other first-principles methods, the sheer quantity of data (e.g., trajectories) generated in AIMD simulations is considerable. Though MSD and other analyses can be performed directly from the raw outputs of the calculations, a more modern approach is to use state-of-the-art databases for data management. In this work, we use MongoDB,⁵¹ a NoSQL database to store the trajectories and analyses from AIMD simulations. Each MD snapshot, together with identifying information and the time step number, is stored as a single document within a collection. This storage scheme allows one to efficiently query for subsets of snapshots (e.g., every 10 or 100 time steps) for analysis. The results of all analyses (e.g., calculated diffusivities, conductivities, activation barriers, etc.) are stored in a separate collection for easy retrieval. Samples of BSON (Binary Javascript Object Notation) dumps of the MongoDB documents for 100 trajectories and the analysis of $\text{Li}_6\text{PS}_5\text{Cl}$ are given in Text File 1 and Text File 2, respectively.

Example. The Li^+ diffusion analyses for $\text{Li}_6\text{PS}_5\text{Cl}$ are given in Notebook 3. Figure 6 shows the Arrhenius plot for $\text{Li}_6\text{PS}_5\text{Cl}$

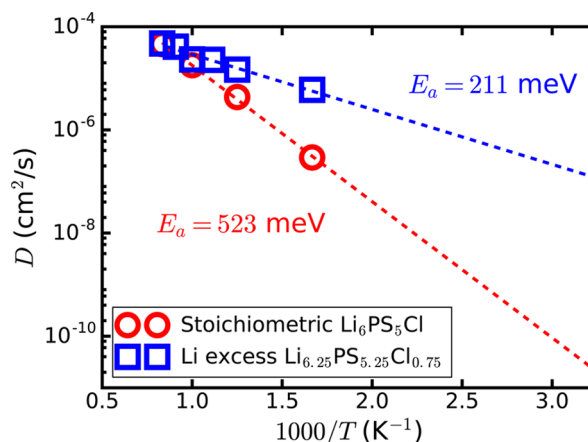


Figure 6. Arrhenius plots for stoichiometric $\text{Li}_6\text{PS}_5\text{Cl}$ (red) and Li excess $\text{Li}_{6.25}\text{PS}_{5.25}\text{Cl}_{0.75}$ (blue). The standard deviations of E_a for stoichiometric $\text{Li}_6\text{PS}_5\text{Cl}$ and Li excess $\text{Li}_{6.25}\text{PS}_{5.25}\text{Cl}_{0.75}$ are 13 and 18 meV, respectively.

with diffusivities computed at four elevated temperatures (600 to 1200 K with 200 K increments). We find that stoichiometric $\text{Li}_6\text{PS}_5\text{Cl}$ is a poor ionic conductor ($\sigma_{300\text{ K}} \approx 2 \times 10^{-3}$ mS/cm) with a high activation energy (E_a) of 524 meV.

The experimentally reported crystal structure has formula $\text{Li}_{6.72}\text{PS}_5\text{Cl}$, i.e., excess of Li. To more accurately model the reported phase, we performed similar analyses on a $\text{Li}_{6.25}\text{PS}_{5.25}\text{Cl}_{0.75}$ cell, which was constructed by introducing a single Li^+ excess into the ordered stoichiometric $\text{Li}_6\text{PS}_5\text{Cl}$ conventional cell with a Cl^- substituted by a S^{2-} to ensure overall charge neutrality. The Li excess $\text{Li}_{6.25}\text{PS}_{5.25}\text{Cl}_{0.75}$ structure is only slightly less stable ($E_{\text{hull}} = 27$ meV/atom) than the stoichiometric $\text{Li}_6\text{PS}_5\text{Cl}$ at 0 K. In terms of transport properties, Li excess $\text{Li}_{6.25}\text{PS}_{5.25}\text{Cl}_{0.75}$ exhibits a much higher room temperature ionic conductivity of 14 mS/cm and a much lower activation energy of 211 meV (Figure 6). The predicted room-temperature ionic conductivity is about 1 order of magnitude higher than previously measured total conductivities for this ASIC. The predicted activation energy is in reasonable

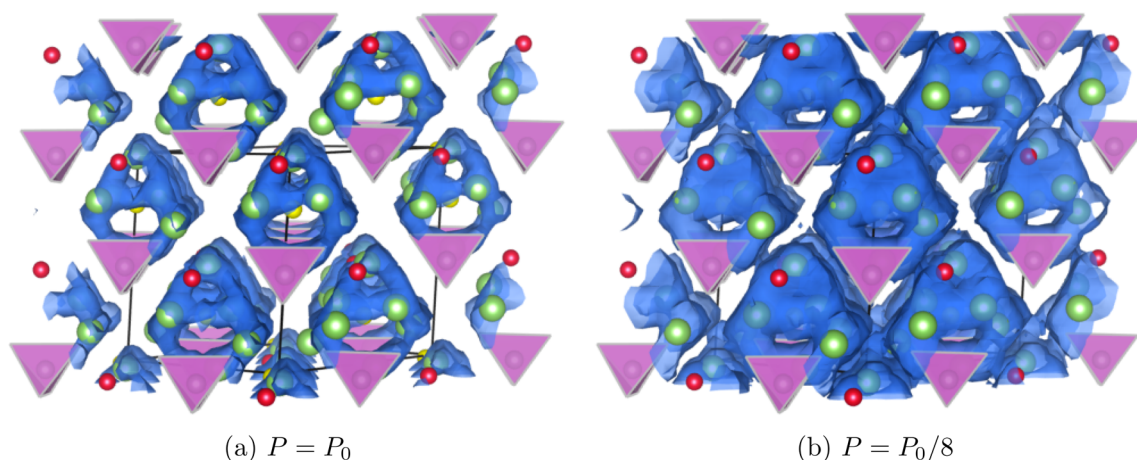


Figure 7. Li^+ probability density distribution in Li excess $\text{Li}_{6.25}\text{PS}_{5.25}\text{Cl}_{0.75}$ obtained from AIMD simulations at 800 K. Isosurfaces (blue) of ionic probability densities are plotted at isovalues of P_0 and $P_0/8$, where $P_0 = 0.0025/a_0^3$ (a_0 is the Bohr radius).

agreement with the experimentally reported values, though it should be noted that reported experimental values vary widely due to variations in the synthesis conditions and compositions.^{24,25}

Figure 7 shows the Li^+ probability density function (PDF) for Li excess $\text{Li}_{6.25}\text{PS}_{5.25}\text{Cl}_{0.75}$ at 800 K at various isovalues. We may observe from the PDF at higher isovalue (Figure 7a) that Li^+ tends to move in a cage-like environment around each S 4d site, forming distorted Li_6S octahedrons. These results are similar to those reported in a previous study using bond valence methods.^{24,25} Because the cage-like trajectory is localized around a particular S site, this type of migration does not contribute to long-range ionic diffusion. Long-range diffusion happens due to migration between different cages, which can be observed at lower isovalues (Figure 7b).

The upper two plots in Figure 8 show the G_s for stoichiometric $\text{Li}_6\text{PS}_5\text{Cl}$ and Li excess $\text{Li}_{6.25}\text{PS}_{5.25}\text{Cl}_{0.75}$, respectively. We observe that there is a persistent peak in G_s between 3.5 and 4.5 Å, which corresponds to the nearest Li–Li distances within the same cage, in both cases. However, this cage-related peak decays much more rapidly in the case of Li

excess $\text{Li}_{6.25}\text{PS}_{5.25}\text{Cl}_{0.75}$ compared to stoichiometric $\text{Li}_6\text{PS}_5\text{Cl}$, and additional peaks at larger r values appear after ~ 30 ps. From the G_d plots (lower plots in Figure 8), we find that there is a high probability of a vacated Li site being rapidly occupied by another Li^+ , though the time scale of these events is much shorter in the case of $\text{Li}_{6.25}\text{PS}_{5.25}\text{Cl}_{0.75}$, which is consistent with the faster diffusion observed in the Li excess material.

DISCUSSION

In this work, we present a detailed outline of how an ASIC can be comprehensively evaluated for multiple critical properties of interest using first-principles calculations combined with modern IT infrastructure and software tools. The first-principles calculations in themselves are not novel and have been used in many previous works, albeit on a more limited scale. However, the use of modern IT infrastructure and software tools dramatically transforms the efficiency and scale in which such investigations can be carried out. Using relatively modest computational resources and the infrastructure outlined, we have performed an assessment of more than 200 compositions for ASIC applications within the space of two years.

Most of the techniques are readily extendable to other applications. For instance, phase stability analysis is a common requirement for most materials design problems, and we have demonstrated how such assessments can be carried out with minimal DFT computational effort and the use of existing large online databases. The alkali grand potential phase diagram analysis shows that some complex interfacial problems can be approximated by considering the relative species mobilities, though an accurate assessment of interfacial reactivity would require more complicated techniques, e.g., MD interfacial simulations with first-principles methods or reactive force fields. Finally, AIMD simulations present a data management challenge that can be effectively managed with modern databases and sophisticated analysis techniques.

As a case study, we have demonstrated how all these techniques may be applied to argyrodite $\text{Li}_6\text{PS}_5\text{Cl}$. Well-documented notebooks showing all the analyses are provided in the Supporting Information, which may serve as a template for similar analyses of other systems. We find stoichiometric $\text{Li}_6\text{PS}_5\text{Cl}$ to be a metastable, poor ionic conductor with limited intrinsic electrochemical stability, not unlike other thiophosphate ASICs.^{4,52} Ionic conductivity is dramatically enhanced

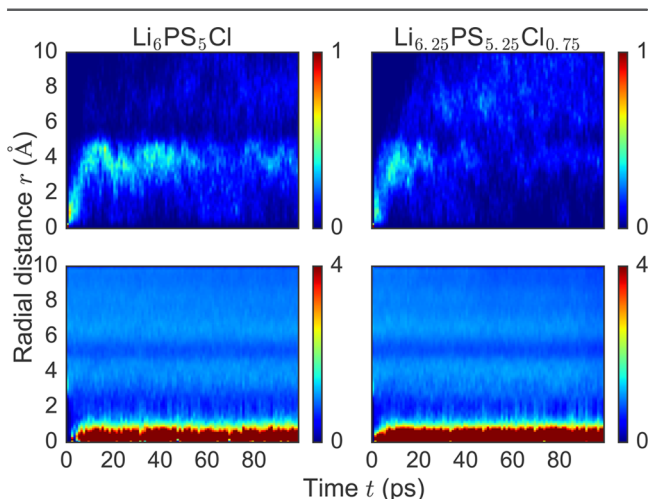


Figure 8. Plots of the self G_s (upper) and distinct G_d (lower) parts of the van Hove correlation function for stoichiometric $\text{Li}_6\text{PS}_5\text{Cl}$ (left) and Li excess $\text{Li}_{6.25}\text{PS}_{5.25}\text{Cl}_{0.75}$ (right) obtained from AIMD simulations at 800 K.

with the introduction of excess Li, and electrochemical stability is achieved via the formation of electronically insulating, ionically conducting passivation phases.

The most interesting feature about argyrodite $\text{Li}_6\text{PS}_5\text{Cl}$ with and without Li excess is the existence of cage-like trapping of Li ions, a feature that can readily be observed in the van Hove correlation and probability density function analyses. Indeed, stoichiometric $\text{Li}_6\text{PS}_5\text{Cl}$ exhibits low Li^+ conductivity and high effective activation barriers in the AIMD simulations as motions within these cages do not contribute to long-range diffusivity. The introduction of Li excess increases the occupancy of the interstitial sites and promotes interstage mobility, resulting in predicted conductivities and activation barriers that are much closer to experimentally observed values.^{24,25} Similar alkali-excess-induced diffusion has been predicted in the cubic Na_3PS_4 superionic conductor.⁹

The predicted conductivity of 14 mS/cm for Li excess $\text{Li}_{6.25}\text{PS}_{5.25}\text{Cl}_{0.75}$ is about an order of magnitude higher than experimentally observed values of 1.1 mS/cm.^{24,25} There are three possible reasons for this discrepancy. First, there is uncertainty in the extrapolated conductivity (12–18 mS/cm) due to the statistical nature of AIMD simulations, which is magnified by the Arrhenius nature of the D vs $1/T$ relationship. Second, the experimentally reported values are for total conductivities, which are not directly comparable to the bulk conductivities computed in our simulations. This suggests that there may be a scope for further enhancement of the conductivity via composition tuning or synthesis optimization to reduce grain boundary resistance.²¹ Finally, the limited cell sizes used in AIMD simulations ($1 \times 1 \times 1$ conventional cell) may also lead to overestimated ionic conductivity due to artificial correlated diffusivity introduced by the periodic boundary conditions. However, a simulation cell size of ~ 10 Å in each direction usually yields reasonable diffusion estimates, as it is typically larger than correlation length scales.¹⁸ Further convergence tests are not within the scope of this manuscript due to the high computational cost involved in simulating a $2 \times 2 \times 2$ cell (416 atoms).

CONCLUSION

To conclude, this work presents a detailed outline of how first-principles methods combined with modern IT infrastructure and software codes can be used to efficiently study and design alkali superionic conductors. The focus is on a holistic assessment of desired superionic conductor properties, including phase and electrochemical stability as well as ionic conductivity. The demonstrated techniques are codified in well-documented, reusable Jupyter notebooks that can be extended to other materials systems and design problems. Using the argyrodite $\text{Li}_6\text{PS}_5\text{Cl}$ superionic conductor as a case study, we discuss the insights gained into the critical role that Li excess plays in enhancing its Li^+ conductivity.

ASSOCIATED CONTENT

Supporting Information

The Supporting Information is available free of charge on the ACS Publications website at DOI: [10.1021/acs.chemmater.6b02648](https://doi.org/10.1021/acs.chemmater.6b02648).

Example Jupyter notebooks (HTML format for preview available) with data files required (ZIP)

Sample BSON dumps of MongoDB documents for 100 trajectories (TXT)

Sample BSON dump of MongoDB document for analysis of $\text{Li}_6\text{PS}_5\text{Cl}$ (TXT)

AUTHOR INFORMATION

Corresponding Author

*E-mail: ongsp@eng.ucsd.edu.

Notes

The authors declare no competing financial interest.

ACKNOWLEDGMENTS

This work was supported by the U.S. Department of Energy, Office of Science, Basic Energy Sciences under Award No. DE-SC0012118. We also acknowledge computational resources provided by Triton Shared Computing Cluster (TSCC) at the University of California, San Diego, the National Energy Research Scientific Computing Center (NERSC), and the Extreme Science and Engineering Discovery Environment (XSEDE) supported by National Science Foundation under Grant No. ACI-1053575.

REFERENCES

- (1) Knauth, P. Inorganic solid Li ion conductors: An overview. *Solid State Ionics* **2009**, *180*, 911–916.
- (2) Takada, K. Progress and prospective of solid-state lithium batteries. *Acta Mater.* **2013**, *61*, 759–770.
- (3) Pan, H.; Hu, Y.-S.; Chen, L. Room-temperature stationary sodium-ion batteries for large-scale electric energy storage. *Energy Environ. Sci.* **2013**, *6*, 2338.
- (4) Kamaya, N.; Homma, K.; Yamakawa, Y.; Hirayama, M.; Kanno, R.; Yonemura, M.; Kamiyama, T.; Kato, Y.; Hama, S.; Kawamoto, K.; Mitsui, A. A lithium superionic conductor. *Nat. Mater.* **2011**, *10*, 682–686.
- (5) Bron, P.; Johansson, S.; Zick, K.; auf der G nne, J. S.; Dehnen, S. S.; Roling, B. $\text{Li}_{10}\text{SnP}_2\text{S}_{12}$: An Affordable Lithium Superionic Conductor. *J. Am. Chem. Soc.* **2013**, *135*, 15694–15697.
- (6) Kuhn, A.; Gerbig, O.; Zhu, C.; Falkenberg, F.; Maier, J.; Lotsch, B. V. A new ultrafast superionic Li-conductor: ion dynamics in $\text{Li}_{11}\text{Si}_2\text{PS}_{12}$ and comparison with other tetragonal LGPS-type electrolytes. *Phys. Chem. Chem. Phys.* **2014**, *16*, 14669–14674.
- (7) Kato, Y.; Hori, S.; Saito, T.; Suzuki, K.; Hirayama, M.; Mitsui, A.; Yonemura, M.; Iba, H.; Kanno, R. High-power all-solid-state batteries using sulfide superionic conductors. *Nat. Energy* **2016**, *1*, 16030.
- (8) Hayashi, A.; Noi, K.; Sakuda, A.; Tatsumisago, M. Superionic glass-ceramic electrolytes for room-temperature rechargeable sodium batteries. *Nat. Commun.* **2012**, *3*, 856.
- (9) Zhu, Z.; Chu, I.-H.; Deng, Z.; Ong, S. P. Role of Na^+ Interstitials and Dopants in Enhancing the Na^+ Conductivity of the Cubic Na_3PS_4 Superionic Conductor. *Chem. Mater.* **2015**, *27*, 8318–8325.
- (10) Zhang, L.; Yang, K.; Mi, J.; Lu, L.; Zhao, L.; Wang, L.; Li, Y.; Zeng, H. Na_3PSe_4 : A Novel Chalcogenide Solid Electrolyte with High Ionic Conductivity. *Adv. Energy Mater.* **2015**, *5*, 1501294.
- (11) Bo, S.-H.; Wang, Y.; Kim, J. C.; Richards, W. D.; Ceder, G. Computational and Experimental Investigations of Na-Ion Conduction in Cubic Na_3PSe_4 . *Chem. Mater.* **2016**, *28*, 252–258.
- (12) Murugan, R.; Thangadurai, V.; Weppner, W. Fast lithium ion conduction in garnet-type $\text{Li}_7\text{La}_3\text{Zr}_2\text{O}_{12}$. *Angew. Chem., Int. Ed.* **2007**, *46*, 7778–7781.
- (13) Inaguma, Y.; Liqun, C.; Itoh, M.; Nakamura, T.; et al. High Ionic Conductivity in Lithium Lanthanum Titanate. *Solid State Commun.* **1993**, *86*, 689–693.
- (14) Goodenough, J. B.; Hong, H. Y.-P.; Kafalas, J. A. Fast Na^+ -ion Transport in Skeleton Structures. *Mater. Res. Bull.* **1976**, *11*, 203–220.
- (15) Meng, Y. S.; Arroyo-de Dompablo, M. E. First principles computational materials design for energy storage materials in lithium ion batteries. *Energy Environ. Sci.* **2009**, *2*, 589.

- (16) Ceder, G.; Hautier, G.; Jain, A.; Ong, S. P. Recharging lithium battery research with first-principles methods. *MRS Bull.* **2011**, *36*, 185–191.
- (17) Deng, Z.; Mo, Y.; Ong, S. P. Computational studies of solid-state alkali conduction in rechargeable alkali-ion batteries. *NPG Asia Mater.* **2016**, *8*, e254.
- (18) Mo, Y.; Ong, S. P.; Ceder, G. First Principles Study of the $\text{Li}_{10}\text{GeP}_2\text{S}_{12}$ Lithium Super Ionic Conductor Material. *Chem. Mater.* **2012**, *24*, 15–17.
- (19) Ong, S. P.; Mo, Y.; Richards, W. D.; Miara, L.; Lee, H. S.; Ceder, G. Phase stability, electrochemical stability and ionic conductivity of the $\text{Li}_{10\pm1}\text{MP}_2\text{X}_{12}$ ($\text{M} = \text{Ge, Si, Sn, Al}$ or P , and $\text{X} = \text{O, S}$ or Se) family of superionic conductors. *Energy Environ. Sci.* **2013**, *6*, 148–156.
- (20) Deng, Z.; Radhakrishnan, B.; Ong, S. P. Rational Composition Optimization of the Lithium-Rich $\text{Li}_3\text{OCl}_{1-x}\text{Br}_x$ Anti-Perovskite Superionic Conductors. *Chem. Mater.* **2015**, *27*, 3749–3755.
- (21) Chu, I.-H.; Nguyen, H.; Hy, S.; Lin, Y.-C.; Wang, Z.; Xu, Z.; Deng, Z.; Meng, Y. S.; Ong, S. P. Insights into the Performance Limits of the $\text{Li}_7\text{P}_3\text{S}_{11}$ Superionic Conductor: A Combined First-Principles and Experimental Study. *ACS Appl. Mater. Interfaces* **2016**, *8*, 7843–7853.
- (22) Deiseroth, H.-J.; Kong, S.-T.; Eckert, H.; Vannahme, J.; Reiner, C.; Zaiß, T.; Schlosser, M. $\text{Li}_6\text{PS}_5\text{X}$: A class of crystalline Li-rich solids with an unusually high Li^+ mobility. *Angew. Chem., Int. Ed.* **2008**, *47*, 755–758.
- (23) Deiseroth, H.-J.; Maier, J.; Weichert, K.; Nickel, V.; Kong, S.-T.; Reiner, C. Li_6PS_5 and $\text{Li}_6\text{PS}_5\text{X}$ ($\text{X} = \text{Cl, Br, I}$): Possible Three-dimensional Diffusion Pathways for Lithium Ions and Temperature Dependence of the Ionic Conductivity by Impedance Measurements. *Z. Anorg. Allg. Chem.* **2011**, *637*, 1287–1294.
- (24) Rao, R. P.; Adams, S. Studies of lithium argyrodite solid electrolytes for all-solid-state batteries. *Phys. Status Solidi A* **2011**, *208*, 1804–1807.
- (25) Rao, R. P.; Sharma, N.; Peterson, V. K.; Adams, S. Formation and conductivity studies of lithium argyrodite solid electrolytes using in-situ neutron diffraction. *Solid State Ionics* **2013**, *230*, 72–76.
- (26) Chen, H. M.; Maohua, C.; Adams, S. Stability and ionic mobility in argyrodite-related lithium-ion solid electrolytes. *Phys. Chem. Chem. Phys.* **2015**, *17*, 16494–16506.
- (27) Fergus, J. W. Electrolytes for solid oxide fuel cells. *J. Power Sources* **2006**, *162*, 30–40.
- (28) Kresse, G.; Furthmüller, J. Efficient iterative schemes for *ab initio* total-energy calculations using a plane-wave basis set. *Phys. Rev. B: Condens. Matter Mater. Phys.* **1996**, *54*, 11169–11186.
- (29) Blöchl, P. E. Projector augmented-wave method. *Phys. Rev. B: Condens. Matter Mater. Phys.* **1994**, *50*, 17953–17979.
- (30) Perdew, J. P. J.; Burke, K.; Ernzerhof, M. Generalized Gradient Approximation Made Simple. *Phys. Rev. Lett.* **1996**, *77*, 3865–3868.
- (31) Ong, S. P.; Richards, W. D.; Jain, A.; Hautier, G.; Kocher, M.; Cholia, S.; Gunter, D.; Chevrier, V. L.; Persson, K. A.; Ceder, G. Python Materials Genomics (pymatgen): A robust, open-source python library for materials analysis. *Comput. Mater. Sci.* **2013**, *68*, 314–319.
- (32) *pymatgen-diffusion*; <http://pypi.python.org/pypi/pymatgen-diffusion>.
- (33) Pérez, F.; Granger, B. E. IPython: A System for Interactive Scientific Computing Python. *Comput. Sci. Eng.* **2007**, *9*, 21–29.
- (34) Bergerhoff, G.; Hundt, R.; Sievers, R.; Brown, I. D. The inorganic crystal structure data base. *J. Chem. Inf. Model.* **1983**, *23*, 66–69.
- (35) Hart, G. L. W.; Forcade, R. W. Algorithm for generating derivative structures. *Phys. Rev. B: Condens. Matter Mater. Phys.* **2008**, *77*, 224115.
- (36) Barber, C. B.; Dobkin, D. P.; Huhdanpaa, H. The quickhull algorithm for convex hulls. *ACM Trans. Math. Softw.* **1996**, *22*, 469–483.
- (37) Ong, S. P.; Wang, L.; Kang, B.; Ceder, G. Li-Fe-P-O₂ Phase Diagram from First Principles Calculations. *Chem. Mater.* **2008**, *20*, 1798–1807.
- (38) Aydinol, M. K.; Kohan, A. F.; Ceder, G.; Cho, K.; Joannopoulos, J. *Ab initio* study of lithium intercalation in metal oxides and metal dichalcogenides. *Phys. Rev. B: Condens. Matter Mater. Phys.* **1997**, *56*, 1354–1365.
- (39) Jain, A.; Ong, S. P.; Hautier, G.; Chen, W.; Richards, W. D.; Dacek, S.; Cholia, S.; Gunter, D.; Skinner, D.; Ceder, G.; Persson, K. A. Commentary: The Materials Project: A materials genome approach to accelerating materials innovation. *APL Mater.* **2013**, *1*, 011002.
- (40) Ong, S. P.; Cholia, S.; Jain, A.; Brafman, M.; Gunter, D.; Ceder, G.; Persson, K. A. The Materials Application Programming Interface (API): A simple, flexible and efficient API for materials data based on REpresentational State Transfer (REST) principles. *Comput. Mater. Sci.* **2015**, *97*, 209–215.
- (41) Jain, A.; Hautier, G.; Ong, S. P.; Moore, C. J.; Fischer, C. C.; Persson, K. A.; Ceder, G. Formation enthalpies by mixing GGA and GGA + *U* calculations. *Phys. Rev. B: Condens. Matter Mater. Phys.* **2011**, *84*, 045115.
- (42) Jónsson, H.; Mills, G.; Jacobsen, K. W. *Nudged elastic band method for finding minimum energy paths of transitions* **1997**, 385.
- (43) Henkelman, G.; Uberuaga, B. P.; Jónsson, H. A climbing image nudged elastic band method for finding saddle points and minimum energy paths. *J. Chem. Phys.* **2000**, *113*, 9901.
- (44) Ong, S. P.; Chevrier, V. L.; Hautier, G.; Jain, A.; Moore, C.; Kim, S.; Ma, X.; Ceder, G. Voltage, stability and diffusion barrier differences between sodium-ion and lithium-ion intercalation materials. *Energy Environ. Sci.* **2011**, *4*, 3680.
- (45) Car, R.; Parrinello, M. Unified Approach for Molecular Dynamics and Density-Functional Theory. *Phys. Rev. Lett.* **1985**, *55*, 2471–2474.
- (46) Wang, Y.; Richards, W. D.; Ong, S. P.; Miara, L. J.; Kim, J. C.; Mo, Y.; Ceder, G. Design principles for solid-state lithium superionic conductors. *Nat. Mater.* **2015**, *14*, 1026.
- (47) Nosé, S. A unified formulation of the constant temperature molecular dynamics methods. *J. Chem. Phys.* **1984**, *81*, 511.
- (48) Hoover, W. G. Canonical dynamics: Equilibrium phase-space distributions. *Phys. Rev. A: At., Mol., Opt. Phys.* **1985**, *31*, 1695–1697.
- (49) Jain, A.; Ong, S. P.; Chen, W.; Medasani, B.; Qu, X.; Kocher, M.; Brafman, M.; Petretto, G.; Rignanese, G.-M.; Hautier, G.; Gunter, D.; Persson, K. A. FireWorks: a dynamic workflow system designed for highthroughput applications. *Concurr. Comput. Pract. Exp.* **2015**, *27*, 5037–5059.
- (50) *custodian*; <http://pypi.python.org/pypi/custodian>.
- (51) MongoDB; <https://www.mongodb.com/>.
- (52) Seino, Y.; Ota, T.; Takada, K.; Hayashi, A.; Tatsumisago, M. A sulphide lithium super ion conductor is superior to liquid ion conductors for use in rechargeable batteries. *Energy Environ. Sci.* **2014**, *7*, 627–631.